Electronic Supplementary Material (ESI) for Journal of Materials Chemistry A.

Electronic Supporting Information

for

Superhydrophobic and Anti-corrosion Strain Sensor for Robust Underwater Applications

Ziyi Dai, Sen Ding, Ming Lei, Shunbo Li, Yi Xu, Yinning Zhou,* and Bingpu Zhou*

Z. Dai, S. Ding, M. Lei, Prof. Y. Zhou, Prof. B. Zhou
Joint Key Laboratory of the Ministry of Education, Institute of Applied Physics and Materials Engineering, University of Macau, Avenida da Universidade, Taipa, Macau 999078, China
E-mail: ynzhou@um.edu.mo, bpzhou@um.edu.mo

Prof. S. Li, Prof. Y. Xu
Key Laboratory of Optoelectronic Technology and Systems, Ministry of Education & Key Disciplines Laboratory of Novel Micro-Nano Devices and System Technology, College of Optoelectronics Engineering, Chongqing University, Chongqing 400044, China

Prof. B. Zhou
Department of Physics and Chemistry, Faculty of Science and Technology, University of Macau, Avenida da Universidade, Taipa, Macau 999078, China

Table of Contents

1. Supplementary Video Captions

Video S1: Real-time record of droplet impact test. The video records the water droplet impact on the surface of the SHSS under the released status (ε = 0%). The SHSS was decorated with microcilia array and swelled by CBNPs and silica nanoparticles before the impact test. The impinging velocity of the 10 μL water droplet was ~0.63 m s^{-1} via freely releasing from a height of 2 cm. A complete droplet bounce was observed without any liquid residual on the sensor surface. The video was sped down by 50× for replay (i.e. 1 s in the video equals 20 ms in real-time).

Video S2: Comparison of droplet impact test. As a comparison, the video records the water droplet impact on the surface of pure microcilia and the microcilia swelled by CBNPs only. The impinging velocity of the 10 μL water droplet was ~0.63 m s^{-1} via freely releasing from a height of 2 cm. When the droplet impinged on the surface decorated with pure microcilia, an instant droplet pinning was observed (the left panel of the video). For the substrate decorated with microcilia array and swelled with CBNPs only, the droplet could easily rebound thanks to the low adhesive property. However, the rebound of the droplet carried some of the CBNPs from the surface that were loosely adhered to the substrate (see **Figure S4** for details also). The video was sped down by 50× for replay (i.e. 1 s in the video equals 20 ms in real-time).

Video S3: Self-cleaning capability of the SHSS. The SHSS was firmly attached to a wood wedge. The insoluble stearic acid particles with larger particle size (left panel) and soluble, small sodium chloride (right panel) particles were loaded to the sample surface as the dirt. With continuous water droplet flushing, all loaded particles can be quickly removed from the surface without residual. After the removal of the particles, the surface still preserves the excellent water repellency without obvious decay.

Video S4: High-speed water jet test on SHSS. The video records the complete reflection of a high-speed water jet from the surface of SHSS. A water jet with a constant speed of 11 m s^{-1} was generated by setting the volumetric flow rate of 60 ml min^{-1} on a syringe pump (Harvard Apparatus, USA). The water jet was applied through a steel pipe with the diameter (D) of ~350 μm. The outlet of the steel pipe was fixed with a vertical distance of 2 mm to the film surface that was under evaluation. According to above parameters, the Weber number is ~580 (see **Supplementary Methods** for the calculation of Weber number).

Video S5: Flexible SHSS with robust superhydrophobicity. The SHSS with the dimension of 5 cm×5 cm was attached to the palm of a volunteer. The demonstration showed the water repellency was maintained after various mechanical deformations, e.g. rubbing, compressing, and squeezing, to the SHSS. The SHSS was also completely immersed into the 0.9% NaCl solution, where we could clearly observe the silver mirror effect and a completely non-wetted surface was preserved.

Video S6: Stability of the SHSS in NaCl solution. The SHSS was attached to the inner wall of a water tank and completely immersed under the 0.9% NaCl solution. A digital multimeter was connected to the terminals of the sensor to measure the electrical resistance in real-time. During the evaluation, periodical finger pressing and rubbing were applied to the surface of the sensor. The video showed that during the finger pressing/rubbing, a silver mirror was existent over the sensor surface, indicating the trapped air layer as well as the preserved superhydrophobicity. Furthermore, after 20 cycles' finger pressing/rubbing, the electrical resistance remained almost unchanged. The results confirm that the SHSS is possible to work without interference from the aqueous surroundings.

Video S7: Superhydrophobic robustness against mechanical damage. The preservation of superhydrophobicity after various mechanical evaluations such as steel wire ball and scalpel abrasion was demonstrated in this video. During the evaluation, the SHSS was fixed on a miniature commercial pressure sensor to record the loaded force in real-time. After the mechanical abrasion, the water jet can still be completely reflected from the surface, which indicates that the capability of water repellency is well preserved.

Video S8: Stability of the SHSS against the organic solvent. In this video, we demonstrated the superhydrophobic and electrical stability of the sensor (dimension of 5 cm×5 cm) when exposed to contamination by the organic solvent. The electrical resistance rose significantly when the sensor was wetted by alcohol (95%). However, the resistance returned to the original value after complete evaporation of the alcohol. We also noticed that the water repellency was not affected by the wetting of alcohol. After complete evaporation of alcohol, the water jet can still be completely reflected from the surface of the sensor without any liquid residual. The video convinces the robustness of the as-prepared device in terms of superhydrophobicity and electrical property.

Video S9: Superhydrophobicity in high temperature water bath. The video recorded the overall silver mirror effect when the SHSS was completely immersed in the water bath with high temperature of ~98.6 °C. After taking out from the water bath, it was observed that no liquid was adhering on the surface. The water jet impact with complete rebound further indicates the preservation of water repellency after the immersion in water with a high temperature.

Video S10: Impact of continuous tap water flushing on the electrical stability and durability of superhydrophobic. Real-time record of the resistance variation of the SHSS with a dimension of 5 cm $\times$ 3 cm when the water column (diameter of ~12 mm) was continuously impinging on the surface. A tap water jet with a constant speed of 1.87 m s^{-1} and Weber number of 574 was generated via setting a volumetric flow rate of 4 l min^{-1}. The video shows that under the water jet impact for nearly half a minute, the electrical resistance of the SHSS remains unaffected. It can also be observed that no liquid was pinning on the surface during the tap water flushing process, indicating the robust superhydrophobicity.

Video S11: Real-time record of the resistance stability of SHSS in air or water. The dimension of the sensor is about 2.8 cm $\times$ 5 cm. The insulated SHSS on both ends of the wire is gradually immersed from the air environment into the 0.9% NaCl solution, where the resistance of SHSS does not change significantly during this process. When the sensor was immersed in the NaCl solution, a silver mirror was observed, which contributed to the reduced contact area between the ionic solvent and the sensor surface to render the stability of the electrical resistance. We also noticed that when the conductive clips were in contact with the NaCl solvent, an obvious resistance decrease occurred. This might be attributed to the electrical conductance increase induced by the ionic solvent when in contact with the clips (circled in yellow in the video). The video confirms that the as-prepared sensor possesses excellent electrical stability without the requirement of additional insulating or encapsulation layer.

Video S12: Influence of water jet during the strain sensing. In the video, a linear stretching to 150% was periodically applied to the SHSS. During the measurement process, a liquid jet was applied to the SHSS surface using a syringe needle. Here, we maintained the liquid injection with a relatively small impinging force to avoid the film deformation by the water jet that might finally result in the resistance variation. The complete rebound of the water jet indicated that the surface superhydrophobicity was maintained during the strain testing process. Furthermore, the measured sensing curve was not obviously affected by the water jet, which convinced that the strain sensor possessed the excellent water repellency to render a stable and reliable signal readout.

Video S13: Strain sensing in air and underwater. In this video, the SHSS was attached to the index finger of a volunteer. The finger bending resulted in the increase of electrical resistance, and the bending duration could be reflected from the signal variations. Furthermore, when the sensor was completely immersed in water, the finger bending could still lead to the electrical resistance variation. The results confirmed that the underwater application would not bring unexpected interference and a reliable signal could be well obtained. After removing from the water tank, a superhydrophobic surface could be preserved without the liquid pinning.

Video S14: Morse code transmission based on SHSS underwater. The SHSS was attached to the index finger joint of a volunteer, and both electrical terminals were connected with a circuit that was designed for Morse code conversion and Bluetooth transmission. When the finger was bent, the peripheral circuit would recognize the increased resistance as the signal source. In principle, we defined the bending duration of < 2 s as the 'dot' for Morse code, otherwise a 'dash' code would be generated correspondingly. The programmed software on the mobile phone can convert the transmitted Morse code signal into readable language. See **Methods** in the main text for the detailed design principle of the circuit and software design. The successful transmission of serial code 'SOS' indicates the potential of the SHSS as wearable sensor or signal emitter for underwater applications.

Video S15: Real-time record of the Morse code communication under high-speed water impact. The SHSS was attached to the finger of a research volunteer. Based on the finger bending, the duration can be controlled and applied to define the signal of 'dot' and 'dash' for Morse code generation. Two different volumetric rates, and thus the impact velocities, were applied to evaluate the stability of the SHSS. The tap water jets with constant speeds of 3.4 m s^{-1} and 5.38 m s^{-1} were generated, with the spot diameter (D) of ~8 mm. According to above parameters, the Weber number is 1266.5 and 3137.7 for the water jet impact in this video.

To obtain the peak force of the water jet, a miniature pressure sensor (ZQ-21A, ZHIQU Precision Instruments) was placed directly under the water column to monitor the real-time impact force from the water jet to the film surface. During the testing process, the maximum recorded impact force was 1.93 N. Consequently, the peak pressure was derived as ~38.4 kPa. It can be observed that under the water jet impact, the Morse code ‘SOS’ can still be stably produced without liquid interference. Furthermore, the video showed the complete water rebound when the high-speed water jet was impacting on the surface of the SHSS, indicating the excellent water repellency of the as-prepared SHSS.

2. Supplementary Methods

2.1 Derivation criterion of the device conductivity

Apart from the monitoring of resistance variation, in this work we also applied the conductivity (σ) to evaluate the electrical stability of the SHSS when exposed to sorts of mechanical and chemical tests. In principle, the conductivity is an electrical parameter used to describe the ease of charge flow in a substance. The standard unit of conductivity σ is Siemens per meter (S m^{-1}), which is the reciprocal of resistivity ρ, that is, σ = 1/ρ.

The electrical resistance, which can be directly measured by the digital multimeter during the evaluation process, is represented by:

$$R = \frac{\rho l}{A}$$

And we thus have:

$$\rho = \frac{RA}{l}$$

where R is the measured resistance, A is the cross-sectional area, and *l* is the length of the sensor under evaluation. We finally obtain the value of the conductivity as

$$\sigma = \frac{l}{RA}$$

With the above formula, the conductivity from a specific SHSS can be monitored depending on the measured resistance and the dimensional parameters of the device under investigation. For example, for a SHSS with length (*l*) of 5 cm, cross-sectional area (A) of 1 cm$\times$200 µm, and recorded resistance of ~30 kΩ, the resultant conductivity is ~0.83 S m^{-1}.

2.2. Calculation of the Weber number

The Weber number (We) is applied to define the ratio of the fluid's inertia when compared with the surface tension during the impact test from tap water jet. For the Weber number in this study, it can be written as

$$We = \frac{\rho v^2 l}{\sigma}$$

where ρ is the fluid density (997 kg m^{-3}), υ is the velocity, l is the characteristic length, and σ is the surface tension of water under room temperature (72.75 mN m^{-1}). Herein, l was considered the same as the diameter of the water column where impinging on the surface of the SHSS. To determine the impact velocity of the water jet on the film, we used a container to collect the inbound water at the same level within a specific period, T. With the measured volume (V) of collected water, the impact velocity was roughly calculated as

$$v = \frac{V}{\pi \cdot \left(\frac{l}{2}\right)^2 \cdot T}$$

The Weber number can thus be obtained based on the two formulas above.

3. Supplementary Figures

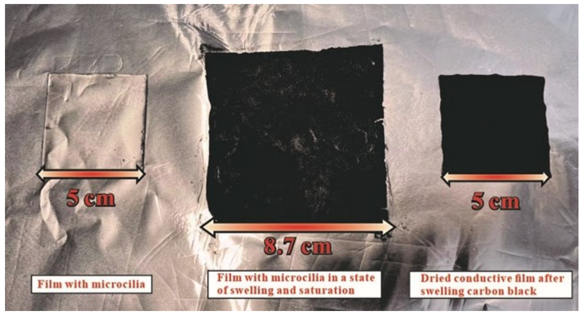

Figure S1. Optical images of the microcilia decorated PDMS film before the swelling process (a); swelled by CBNPs (b); and dried after the swelling process of (c).

The optical images indicate that the swelling process leads to the obvious area variation of the as-prepared film. During this process, it is thus positive for the nanoparticle (CBNPs) penetration into the PDMS matrix. However, after the complete evaporation of the solvents, the area recovered to the initial status before the swelling process. Furthermore, the film color from transparent to completely black convinces the successful penetration of CBNPs onto the PDMS matrix which enables the conductive path for strain sensing.

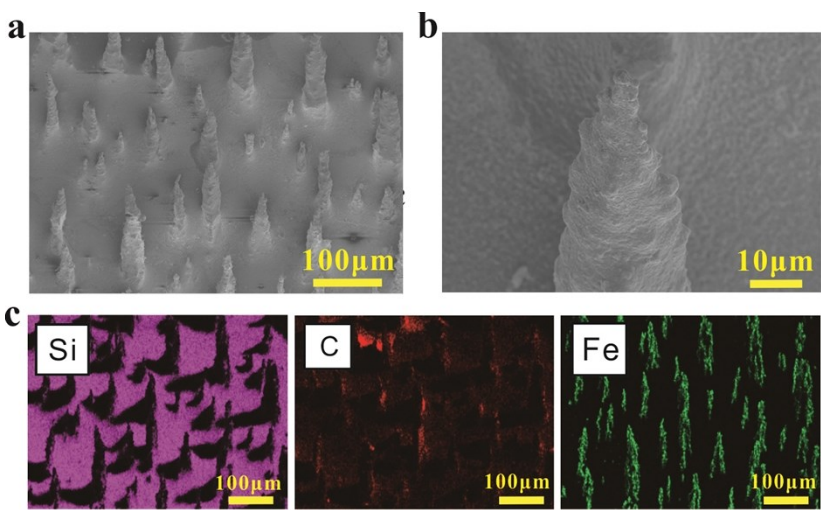

Figure S2. SEM images of (a) The sensor surface for element mapping analysis (EDS) and (b) A typical microcilia after the swelling process of CBNPs and silica nanoparticles. (c) EDS element mapping results of Si, C, and Fe, respectively.

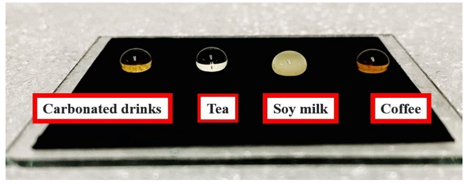

Figure S3. Optical image of the SHSS, with the droplets of carbonated drinks, green tea, soy milk, and coffee. Due to the superhydrophobic surface property, the droplets were resident on top of the SHSS and maintained the spherical shapes without spreading. The volume of all droplets loaded on the SHSS surface is 20 μL.

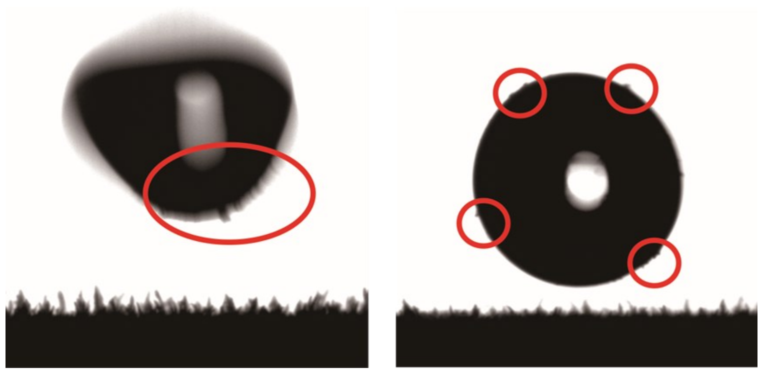

Figure S4. Optical images of the droplet rebound (10 μL) on the PDMS surface. The sample has been decorated with microcilia array and swelled by CBNPs using the standard process as indicated in the main text.

The parts circled in red indicate that the surface of the droplet is covered with CBNPs after contact with the surface. Compared with the phenomenon mentioned in the main text (**Figure 1e**), the second step of swelling process thus decorates the silica nanoparticles and removes the loosely adhered CBNPs from the substrate at the same time.

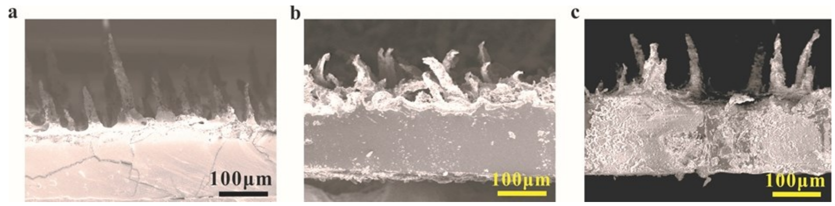

Figure S5. Cross-sectional SEM images of (a) the as-prepared microcilia structures; (b) the microcilia structures after CBNPs swelling process in alcohol condition; and (c) the microcilia structures after CBNPs swelling process in cyclohexane condition.

The cross-section was obtained via cutting the sample using a scalpel, which thus provided us the direct observation about the nanoparticle penetration results into the PDMS matrix. As confirmed from the SEM images, the swelling process in cyclohexane led to the successful penetration of CBNPs into the matrix, which finally enabled the conductive path throughout the substrate for strain sensing.

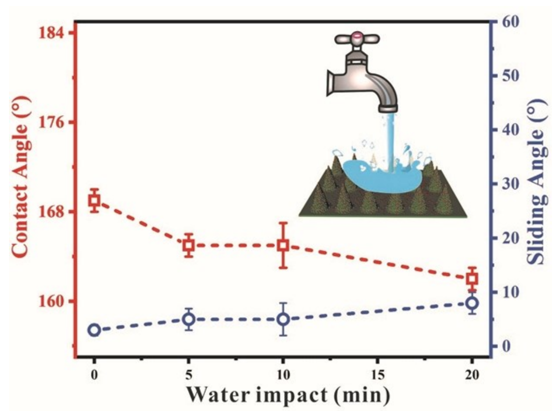

Figure S6. Variations of the contact angle (θ_{CA}) and sliding angle (θ_{SA}) of the SHSS when exposed to continuous tap water flushing with duration up to 20 min. See **Methods** for detailed setup and parameters. The error bars were obtained from distinct measurements via randomly selecting five different positions on a typical sample.

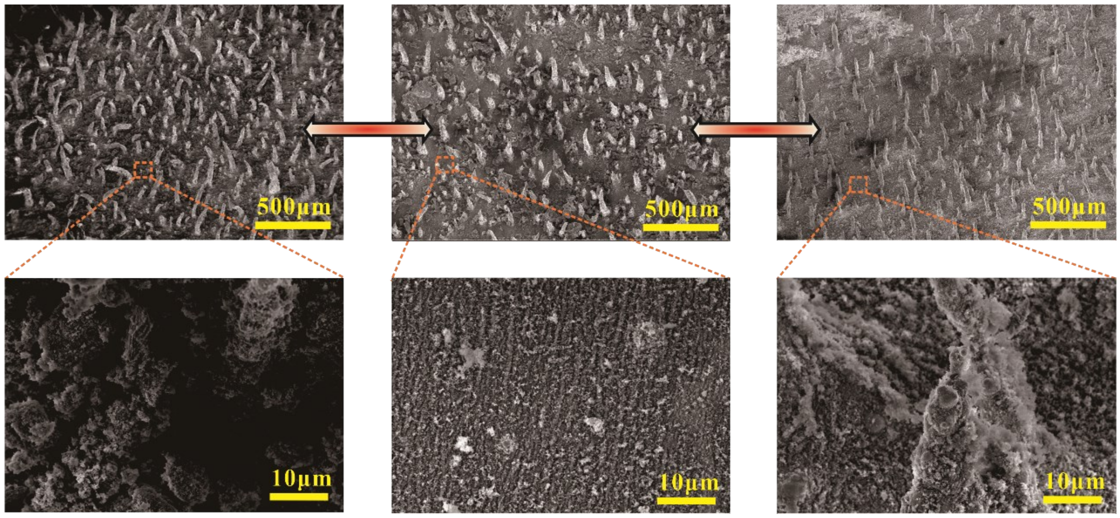

Figure S7. SEM images of the SHSS when exposed to different extents of linear stretching (from left to right: 0%, 100%, and 250%). The SEM images in the lower panels are related to the bottom areas uncovered by the microcilia. The results indicated that the dense microcilia array were formed even under the stretched status, thus leading to the reduced contact area between the loaded droplets and the substrate surface to preserve the superhydrophobicity.

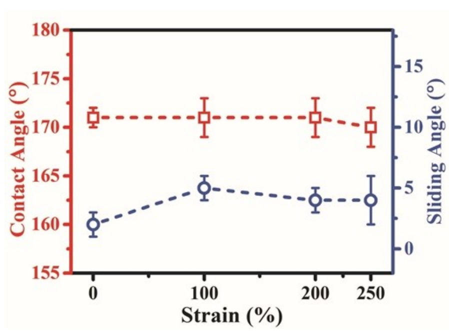

Figure S8. Variations of the contact angle (θ_{CA}) and sliding angle (θ_{SA}) of the SHSS when exposed to different extents (100%, 200%, and 250%) of linear stretching.

A slight decrease of θ_{CA} from 171° to 170° and slight increase of θ_{SA} from 2° to 4° were found, revealing the preserved superhydrophobicity covering the working spectrum. The error bars were obtained from distinct measurements via randomly selecting five different positions on a typical sample.

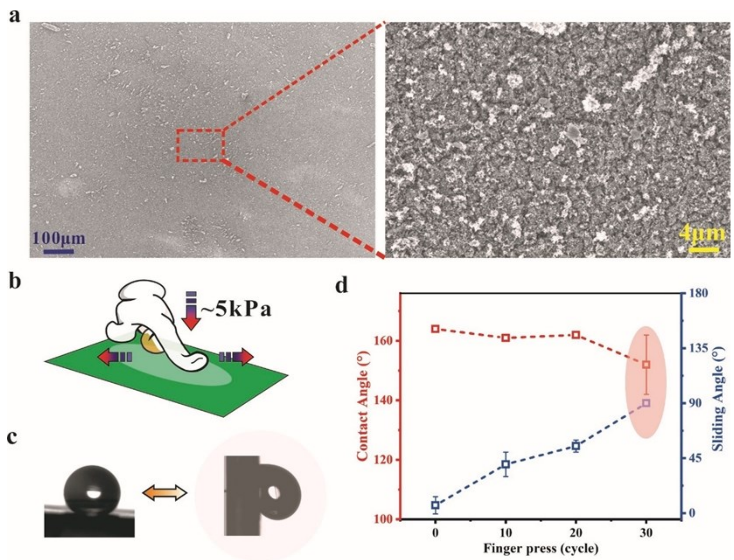

Figure S9. (a) SEM image of the PDMS film without microcilia while swelled with CBNPs and silica nanoparticles successively. (b) Schematic diagram of finger press on the film. (c) Droplet pinning effect after 30 cycles' finger pressing. (d) Variation of θ_{CA} and θ_{SA} after cyclic finger press with 5 kPa pressure.

Figure S9 provides the results of finger press evaluation on the substrate that has been swelled with CBNPs and silica nanoparticles, while without the decoration of microcilia array. Even though the surface has been treated with the hydrophobic silica nanoparticles, significant degradation was found after only 10 cycles' finger pressing due to the absence of the microcilia. After 30 cycles, most regions have lost the capability of water repellency, where the water droplet was adhering on the substrate even when the sample has been tilted by 90°. From this perspective, the surface without decoration of microcilia was easy to be dramatically destroyed under the evaluation of finger pressing, which showed that such surface was not suitable for the reliable and practical applications. The results confirm that apart from the silica nanoparticles, the microcilia array is also of great significance to maintain the robust superhydrophobicity.

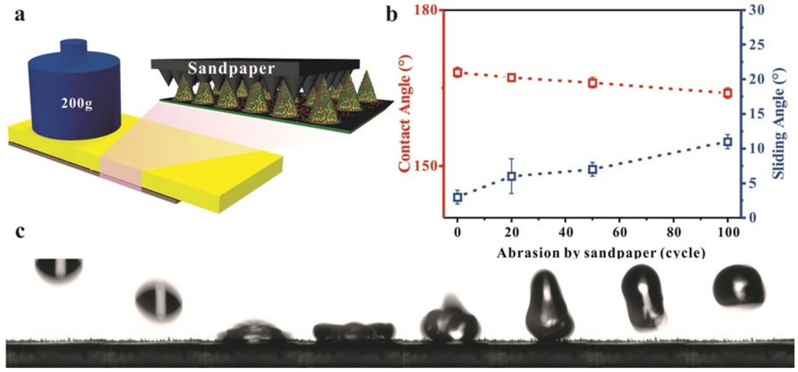

Figure S10. (a) Schematic illustration of the durability test via periodical and lateral mechanical abrasion with a commercial sandpaper (grit #1200). (b) Variation of θ_{CA} and θ_{SA} after cyclic sandpaper abrasions with cycles up to 100. (c) Rebound behavior when the 10 μL droplet was freely released from height of 2 cm towards the surface of the sensor that has been abraded via sandpaper for 100 cycles. The time interval between each optical image is 5 ms.

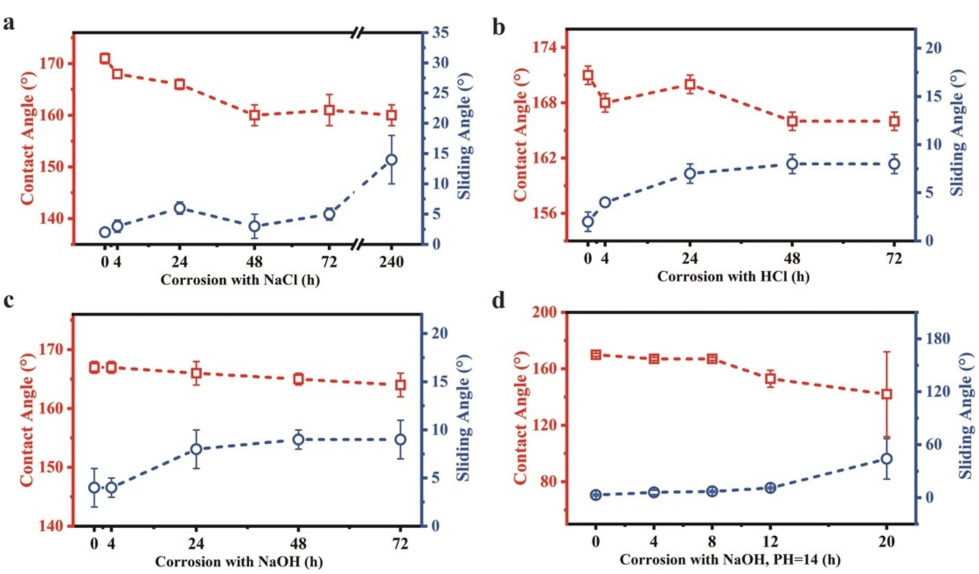

Figure S11. Variations of θ_{CA} and θ_{SA} of the as-prepared SHSS when immersed in (a) 0.9% NaCl solution up to 240 h; (b) HCl solution, PH = 1 up to 72 h; (c) NaOH solution, PH = 12 up to 72 h; and (d) NaOH solution, PH = 14 up to 20 h.

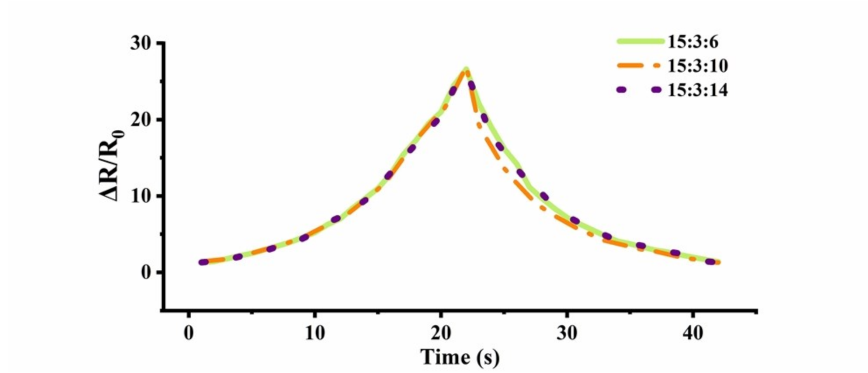

Figure S12. The resistance variation when the SHSS prepared with different CIP ratios was loaded with 150% strain and released.

Herein, the weight ratio of CIP was adjusted to regulate the morphology of the microcilia array. However, the curves indicate that such regulation has insignificant effect on the sensing performance, which means that the main conductive path locates in the substrate matrix. From this perspective, the microcilia array acts as a protective layer and is mainly responsible for the robustness of superhydrophobicity. The main contribution to the conductive path for strain sensing locates in the bulk substrate, which enables the electrical stability of the sensor when exposed to the surface abrasion.

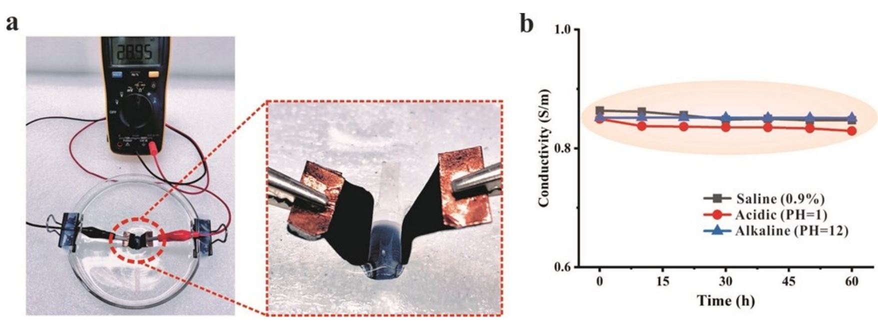

Figure S13. (a) Experimental setup to evaluate the electrical stability of the SHSS when immersed in different solvents such as NaCl, HCl, and NaOH. (b) Variation of the conductivity after the sensor was immersed in different solvents for duration up to 60 h.

To avoid the interference caused by the conductive clips, we fixed the SHSS with a length of 2 cm into the solution for evaluation. During the experiment, the digital multimeter was applied to monitor the variation of the electrical resistance in real-time. The curves showed that the SHSS possessed the conductivity stability when exposed to the solvent corrosion. Furthermore, the silver mirror effect indicated the air pocket layer was successfully formed between the sensor and the solvent to guarantee the electrical stability. For the calculation of the conductivity, please refer to the **Supplementary Methods**.

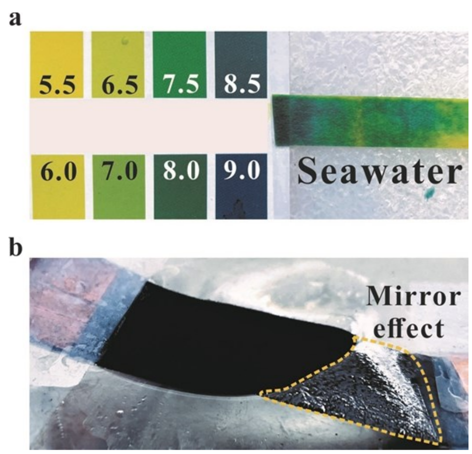

Figure S14. (a) The typical pH value, within the range of 8.0~8.5, of seawater. The seawater was taken from the sea area near Macau. (b) The silver mirror effect of the SHSS when immersed into the seawater, which indicates the existence of trapped air layer between the liquid and the solid surface.

A	B	C	D	E	F	G	H	I	J	K	L	M
• —	— • • •	— • — •	— • •	•	• • — •	— — •	• • • •	• •	• — — —	— • —	• — — —	— —
N	O	P	Q	R	S	T	U	V	W	X	Y	Z
— •	— — —	• — — •	— — • —	• — •	• • •	—	• • —	• • • —	• — —	— • • —	— • — —	— — • •

Figure S15. Benchmarking table of the Morse code system. The combinations of ‘dot’ and ‘dash’ signals were well accepted for the definitions of different letters. In this work, the signals of ‘dot’ and ‘dash’ were generated by controlling the finger bending duration when the sensor was attached to the finger joint of the volunteer.

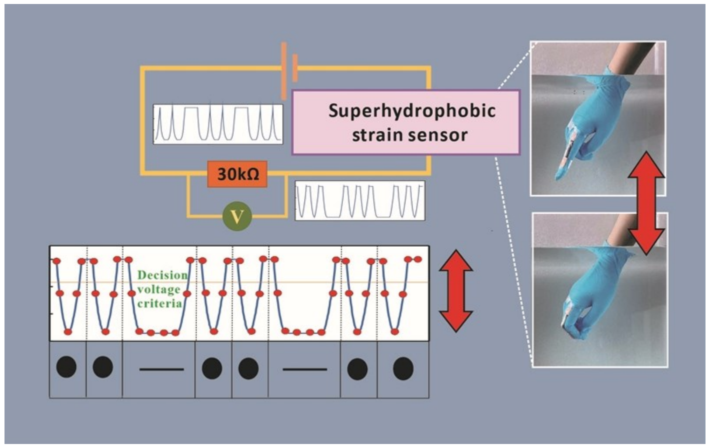

Figure S16. Schematic diagram showing the principle for Morse code generation and conversion based on the SHSS.

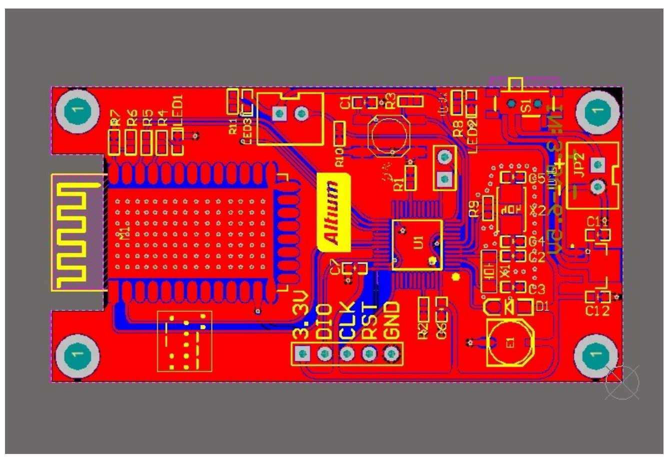

Figure S17. Integrated circuit of Morse code translation and Bluetooth function based on the Altium Designer 13.

Figure S18. The Optical picture of the optical contact angle and sliding angle measurement system. The inset shows the resident water droplet on the sample that is under evaluation.

4. Supplementary Tables

Supplementary Table S1. Consumable cost for the production of SHSS.

Item	Unit Price (USD)	Consumption	Total Price (USD)
PDMS substrate	145 kg^{-1}	0.83 g	0.12
PDMS film	145 kg^{-1}	0.48 g	0.07
Carbonyl iron particle	350 kg^{-1}	0.27 g	0.10
Cyclohexane	10 l^{-1}	70 ml	0.7
Silica nanoparticle	350 kg^{-1}	0.2 g	0.07
Total Cost (5 cm × 5 cm)			1.06
Standard SHSS (1 cm × 5 cm)			0.21

The table (**Table S1**) above shows the rough cost that is required to prepare the superhydrophobic strain sensor with dimension of 5 cm × 1 cm in this work. The unit price is based on the consumable quotation provided via the local suppliers. Estimated consumable expense is considered as the main contribution to account for the cost of production. The consumptions of PDMS and carbonyl iron particles also include the parts wasted during the spin-coating process.

Supplementary Table

Maximum working strain	Maximum GF	Durability	Sandpaper abrasion		Water impact		Chemical corrosion						Fluorinated	Underwater test	Ref
			C*	S*	C	S	Acid		Alkaline		Salt				
							C	S	C	S	C	S			
100%	10E8	1000 (100%)	40 cycles @20g	40cycles @20g	45s	45s	×	droplet	×	droplet	×	droplet	Yes	No	[1]
0.7%	7.5	1000 (0.6%)	×	×	×	×	×	48h	×	48h	×	48h	No	No	[2]
60%	3.6E8	2000 (30%)	60 cycles @20g	60cycle @20g	×	×	×	×	×	×	×	×	No	No	[3]
100%	242.6	1000 (50%)	200 cycles @unmarked (0.01 to 0.001)	30cycles @unmarked	×	×	8h	8h	×	droplet	×	droplet	No	No	[4]
300%	13000	1000(20%)	×	×	×	×	×	×	×	×	×	×	No	No	[5]
100%	0.93	700 (50%)	×	×	×	×	6h	6h	×	droplet	×	droplet	No	No	[6]
100%	5.9	600(50%)	×	×	×	×	6h	droplet	6h with significant changes	droplet	6h	droplet	No	No	[7]
80%	0.6	5000 (10%)	3 cycles @ 3.5 kPa (△R/R$_0$=150%)	×	×	×	×	×	×	×	×	×	No	Yes	[8]
170%	1900	1000 (40%)	×	×	×	×	×	droplet	×	droplet	×	droplet	Yes	No	[9]
100%	21	1000 (50%)	×	×	×	×	droplet (with decay)	8h	droplet	6h (with decay)	droplet (with decay)	8h	Yes	No	[10]
200%	21	10000(10%)	80cycles@500g (with decay)	80cycles@500g	×	200s	24h (with decay)	24h	24h (with decay)	24h	24h	24h	Yes	No	[11]
250%	276	10000 (150%)	100cycle@200g	100cycle@200g	1200s	1200s	72h	72h	72h	72h	240h	240h	No	Yes	This work

C: conductivity; S: superhydrophobicity.

5. Supplementary References

[1] L. Wang, H. Wang, X.-W. Huang, X. Song, M. Hu, L. Tang, H. Xue, J. Gao, *J. Mater. Chem. A,* 2018, **6**, 24523.

[2] Q. Li, H. Liu, S. Zhang, D. Zhang, X. Liu, Y. He, L. Mi, J. Zhang, C. Liu, C. Shen, *ACS Appl. Mater. Interfaces,* 2019, **11**, 21904.

[3] L. Wang, J. Luo, Y. Chen, L. Lin, X. Huang, H. Xue and J. Gao, *ACS Appl. Mater. Interfaces*, 2019, **11**, 17774-17783.

[4] Y. Chen, L. Wang, Z. Wu, J. Luo, B. Li, X. Huang, H. Xue, J. Gao, *Compos. B. Eng.*, 2019, **176**.

[5] D. Yao, L. Wu, S. Peng, X. Gao, C. Lu, Z. Yu, X. Wang, C. Li, Y. He, *ACS Appl. Mater. Interfaces*, 2021.

[6] L. Wang, Y. Chen, L. Lin, H. Wang, X. Huang, H. Xue, J. Gao, *Chem. Eng. J.* , 2019, **362**, 89.

[7] J. Gao, B. Li, X. Huang, L. Wang, L. Lin, H. Wang, H. Xue, *Chem. Eng. J.*, 2019, **373**, 298.

[8] B. N. Sahoo, J. Woo, H. Algadi, J. Lee, T. Lee, *Adv. Mater. Technol.*, 2019, **4**, 1900230.

[9] J. Lin, X. Cai, Z. Liu, N. Liu, M. Xie, B. Zhou, H. Wang, Z. Guo, *Adv. Funct. Mater.*, 2020, **30**, 2000398.

[10] B. Li, J. Luo, X. Huang, L. Lin, L. Wang, M. Hu, L. Tang, H. Xue, J. Gao, Y.-W. Mai, *Compos. B. Eng.*, 2020, **181**, 107580.

[11] P. Wang, W. Wei, Z. Li, W. Duan, H. Han, Q. Xie, *J. Mater. Chem. A*, 2020, **8**, 3509.